An analysis of the cross-borehole GPR tomography for imaging the development of the infiltrated fluid plume

2011 J. Geophys. Eng. 8 294

(http://iopscience.iop.org/1742-2140/8/2/014)

IOP PUBLISHING JOURNAL OF GEOPHYSICS AND ENGINEERING

J. Geophys. Eng. **8** (2011) 294–307 doi:10.1088/1742-2132/8/2/014

An analysis of the cross-borehole GPR tomography for imaging the development of the infiltrated fluid plume

Ping-Yu Chang[1,3] **and David Alumbaugh**[2]

[1] Institute of Applied Geoscience, National Taiwan Ocean University, Taiwan, Republic of China
[2] Schlumberger–EMI Technology Center, Richmond, CA, USA

E-mail: pingyuc@mail.ntou.edu.tw and dalumbaugh@richmond.oilfield.slb.com

Received 28 April 2010
Accepted for publication 9 March 2011
Published 12 April 2011
Online at stacks.iop.org/JGE/8/294

Abstract

To analyse the resolution and accuracy of cross-borehole ground penetrating radar (XBGPR) methods in monitoring the variation due to fluid infiltration in the heterogeneous vadose zone, we built a hypothetical two-dimensional model by using the Sandia-Tech Vadose Zone (STVZ) model for unsaturated-flow modelling. The spatial variation in water content provided by the flow modelling was converted to a dielectric constant and electrical conductivity. We then used these parameters in finite-difference time-domain (FDTD) electromagnetic (EM) forward modelling to simulate the response of cross borehole radar surveys with antenna configurations identical to those of the STVZ site. We inverted the synthetic GPR data by using a damped least-squares method with straight ray-path assumptions. The results from the resolution analysis suggest that attenuation within a clay layer is overestimated near the boreholes but underestimated between the boreholes in the inverted images synthesized by FDTD modelling. Compared to the attenuation images, inverted water-content images are more representative of the input model. The inverted attenuation also shows that artefacts such as 'bull's eye' structures appear in the attenuation images. The reason for the poorer resolution and artefacts in the attenuation images concerns the straight-ray assumptions that we made in the inversion to approximate propagation of the EM waves with additional energy loss when they crossed the velocity boundaries. In addition, the clay layer serves as a waveguide when both the transmitter and receiver located in the clay layer and our current inversion algorithm do not account for the waveguide physics. Thus, it is necessary to properly incorporate physics into the inversion algorithms in order to correctly invert for the attenuation.

Keywords: GPR, tomography, attenuation

1. Introduction

Cross-borehole (XB) ground penetrating radar (GPR) is used extensively in groundwater investigations (e.g. Hubbard *et al* 1997, Alumbaugh *et al* 2000, 2002, Binley *et al* 2001, LaBrecque *et al* 2002, Chang *et al* 2004). Because artefacts may be present in the tomograms owing to inadequate data collection, processing procedures or poor inversion hypothesis (e.g. Irving and Knight 2005, Irving *et al* 2007, Johnson *et al* 2007), it is important to examine XBGPR image resolution and accuracy for different field and survey conditions. For instance, Irving *et al* (2007) propose an inversion approach to improve the resolution of XBGPR images with synthesized XBGPR signals from finite-difference (FD) time-domain (TD) electromagnetic (EM) forward modelling. Two newly interested issues are how well the XBGPR imaging method resolves the preferential flow paths and how the hydraulic parameters are estimated accurately through the XBGPR measurements. Techniques coupling GPR forward modelling

[3] Author to whom any correspondence should be addressed.

Table 1. The hydraulic properties for the geological units in the STVZ model.

Unit	Soil type	θ_r	θ_s	α (m^{-1})	N	k_s ($cm\ s^{-1}$)	k_s (m/day)
1	Sand	0.031	0.305	7.33	3.79	1.80×10^{-3}	1.56
2	Sand	0.049	0.318	20.13	1.82	1.25×10^{-3}	1.08
3	Sand	0.05	0.382	3.72	3.78	3.56×10^{-3}	3.08
4	Loamy sand	0.064	0.365	2.34	1.77	8.50×10^{-4}	0.73
5	Clay	0.089	0.461	1.22	1.39	1.31×10^{-4}	0.11

and groundwater flow modelling provide a way to study the issues. Day-Lewis *et al* (2002) use results from a solute transport simulation to generate synthetic radar data that then facilitate the examination of a time-lapse inversion algorithm based on the field experiment. Kowalsky *et al* (2005) utilize a coupled flow modelling and ray-based GPR forward modelling method for the estimation of soil hydraulic and dielectric parameters through joint inversion of GPR and hydrological data. Most of the previous studies use a homogeneous hypothetical model or a fixed model with variable permeability (e.g. Kowalsky *et al* 2005) for the modelling. However, the previous approaches with a uniform or fixed hydrogeological model may not properly represent the groundwater preferential flow introduced by the heterogeneous structures in the subsurface. In this study, we built a layered heterogeneous model based on the real field measurements and lab measurements, and examined how well the XBGPR resolves the infiltrated water plume and flow paths in a time-lapse sense. This approach can help us to better realize the physics issues that may limit the XBGPR resolution for the preferential flow and estimation accuracy of hydraulic parameters. We used both a coupled unsaturated-flow and a FDTD EM forward-modelling method to analyse the resolution of XBGPR images during a dynamic infiltration simulation similar to that at the Sandia-Tech Vadose Zone (STVZ) facility. It should be noted that the purpose of this research is not to reproduce the experiments at the STVZ site exactly, but to use the method and the measured data for examining the resolution of both XBGPR velocity and attenuation tomography, as well as for analysing the results for artefacts that may arise during data processing.

The XBGPR resolution study was conducted in the following steps: first, we built a two-dimensional (2D) vadose zone model for unsaturated-flow modelling with the measured and the estimated hydraulic parameters at the STVZ site. The overall goal was to simulate the water-infiltration experiment. Second, we converted the spatial variation in water content resulting from unsaturated-flow modelling to a dielectric constant and electrical conductivity by using a petrophysical model determined from controlled field and lab experiments (Alumbaugh *et al* 2002, LaBrecque *et al* 2002, Brainard *et al* 2004). In the FDTD EM forward modelling, we used the dielectric-constant and electrical-conductivity parameters to simulate the response of XB radar signals. Third, after processing and inverting the synthetic digital signal data on the basis of a damped least-squares method, we compared inverted tomographic images with the vadose zone model to analyse the image resolution of the XBGPR method. Finally, we synthesized early-time and late-time solute transport models from the results of the unsaturated-flow modelling, and repeated the aforementioned second and third steps in order to analyse the image resolution and accuracy for solute transport in the flow steady-state condition.

2. Unsaturated-flow modelling

2.1. Vadose zone model for the STVZ site

The vadose zone model was built according to the device configurations and laboratory-measured hydraulic properties at the STVZ test site in New Mexico (Brainard *et al* 2004). Hydrus-2D (Simunek and van Genuchten 1999), a two-dimensional (2D) finite-element code, was used for the flow simulation in this research. The region of interest extends from the surface to a depth of 8 m between boreholes SW and NE to correspond to the previous analysis at the STVZ site (Paprocki 2000, Alumbaugh *et al* 2002, Chang *et al* 2006).

Five major hydrogeological units were recognized from the laboratory-measured hydraulic properties (Baker 2002). The arithmetic mean of the hydraulic parameters for samples in the same layer was calculated, and table 1 shows the hydraulic properties consisting of the residual volumetric water content (θ_r), saturated volumetric water content (θ_s), saturated hydraulic conductivity (K_s), air entry value parameter (α), and pore size distribution parameter n of each layer. To obtain simulated soil geometry, we employed XBGPR pre-infiltration tomograms (Alumbaugh *et al* 2002, Chang *et al* 2004) and electrical resistivity tomography images (LaBrecque *et al* 2002) at the STVZ site. Our specific objective was to help build a five-layer hydrogeological model that approximates the conditions at the site.

To avoid interference from the boundaries, we implemented a larger modelling domain (25 m $\times$ 10 m) by extending the properties on the left, right, and bottom edges of the region of interest out to the boundaries of the modelling domain (figure 1). The domain was discretized through the use of rectangular cells. The vertical and horizontal dimensions of each cell were 0.031 25 and 0.125 m, respectively. The top boundary was set to be a no-flow boundary, except at the location of the 3 m long infiltrometer which was located in the centre of the top boundary.

It must be noted that Hydrus-2D does not account for 3D flow and treats the infiltrometer as a 2D, or infinitely long source, into and out of the tomographic plane. For a given infiltration rate, the moisture front produced by a 2D source will move faster within the 2D plane than that

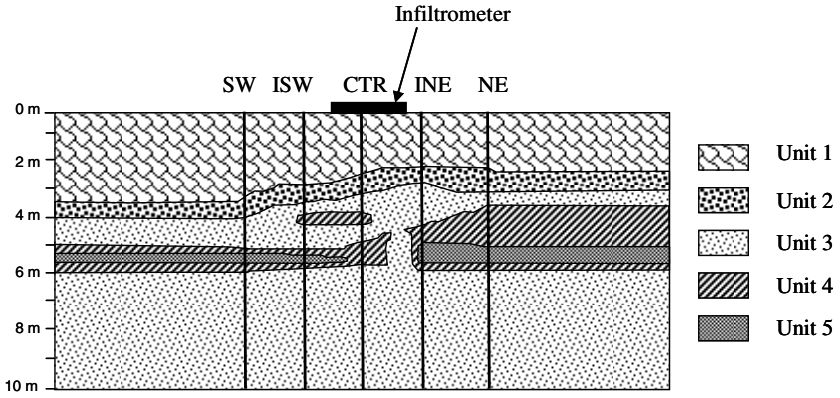

Figure 1. The vadose zone conceptual model, used for the unsaturated-flow modelling at the STVZ site. The solid lines indicate the locations of the XBGPR access boreholes.

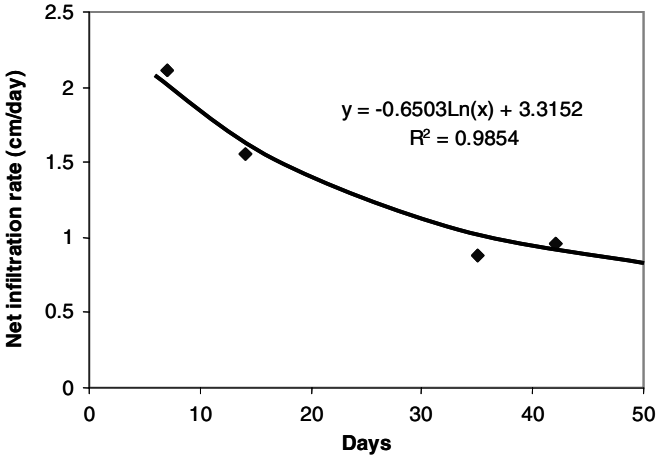

Figure 2. The calculated 2D infiltration rate based on the 2D XBGPR images.

of a 3D source, since no flow out of the plane is allowed. Therefore, the actual infiltration rate of the STVZ infiltrometer (2.7 cm/day) cannot be applied to the 2D model directly. To use Hydrus-2D to simulate infiltration from a finite infiltrometer, we approximated a 2D infiltration rate by using time-varying moisture contents, as derived from the XBGPR images. This estimate first involved calculating how much water was added to the subsurface along the XBGPR profile during a given time period. Then, we calculated the 2D infiltration rate by dividing that value by the length of the infiltrometer (3 m). Afterwards, we chose a variable flux boundary for the infiltrometer by using an interpolated infiltration rate as the input. Figure 2 shows this calculated infiltration rate, which was applied to 2D modelling. The infiltration rate decreases from 2.7 to about 0.8 cm/day in 50 days.

No-flow boundaries were chosen for the lateral boundary. Because the groundwater table is at about 20 m depth at the STVZ site, we assume that the bottom of the vadose zone model is a free drainage boundary. To derive the pre-infiltration conditions, we assigned a uniform water content of 0.1 to the entire model along with a no-flow boundary at the top, and we conducted unsaturated-flow modelling for 6000 days. This steady-state water content was then used as the initial condition for transient-infiltration modelling, which, in turn, ran for 50 days. The resulting water content at day 0, day 7, day 14, day 21, day 35, and day 42 was used for FDTD EM modelling.

2.2. *Results of unsaturated-flow modelling*

Figure 3(*a*) shows the results of the unsaturated-flow modelling of the STVZ model prior to infiltration. These results indicate that the pre-infiltration volumetric water content was as high as 35% in the clay at a depth of 5 to 6 m. The water content was about 20% to 25% in the thin clayey-sand lenses located at a depth of about 4 m. Compared with the clay and the clayey sand, the sand layers contained pre-infiltration water content of less than 10%.

Seven days after the initiation of the infiltration, we found a plume whose water content was greater than 10% above 2 m depth in hydrogeological unit 1. The front of the water plume moved downwards and reached the thin clayey sand at 4 m depth after 14 days of infiltration. A pocket of higher water content (>20%) appeared between a depth of 2 and 3 m within the boundaries of the wetting front at this time. The location of the water pocket corresponded to the depth of unit 2. At day 21, the front of the water plume reached a depth of 6 m, and the water content in the clay (unit 5) surpassed 35%. The simulation had the water plume breaking through the clay layer prior to 35 days after infiltration had begun, and this breakthrough resulted in the front of the water plume reaching depths greater than 7 m after day 35. During this time, the water content in the clay layer at 4 to 6 m depth increased to over 40%.

Owing to the decrease of the infiltration rate, a slight decrease of 5% in the volumetric water content was observable in the water pocket at 2 to 3 m depth in the images of days 35 and 42. It should be noted here that we did not try to mimic the real field conditions, and this phenomenon, based on an approximate 2D infiltration rate, may not actually occur at the STVZ site. The model also indicates a discontinuity in the clay layer at 4 to 6 m depth around the Inner Northeast (INE) borehole in figure 1, with the enhanced moisture plume avoiding this region.

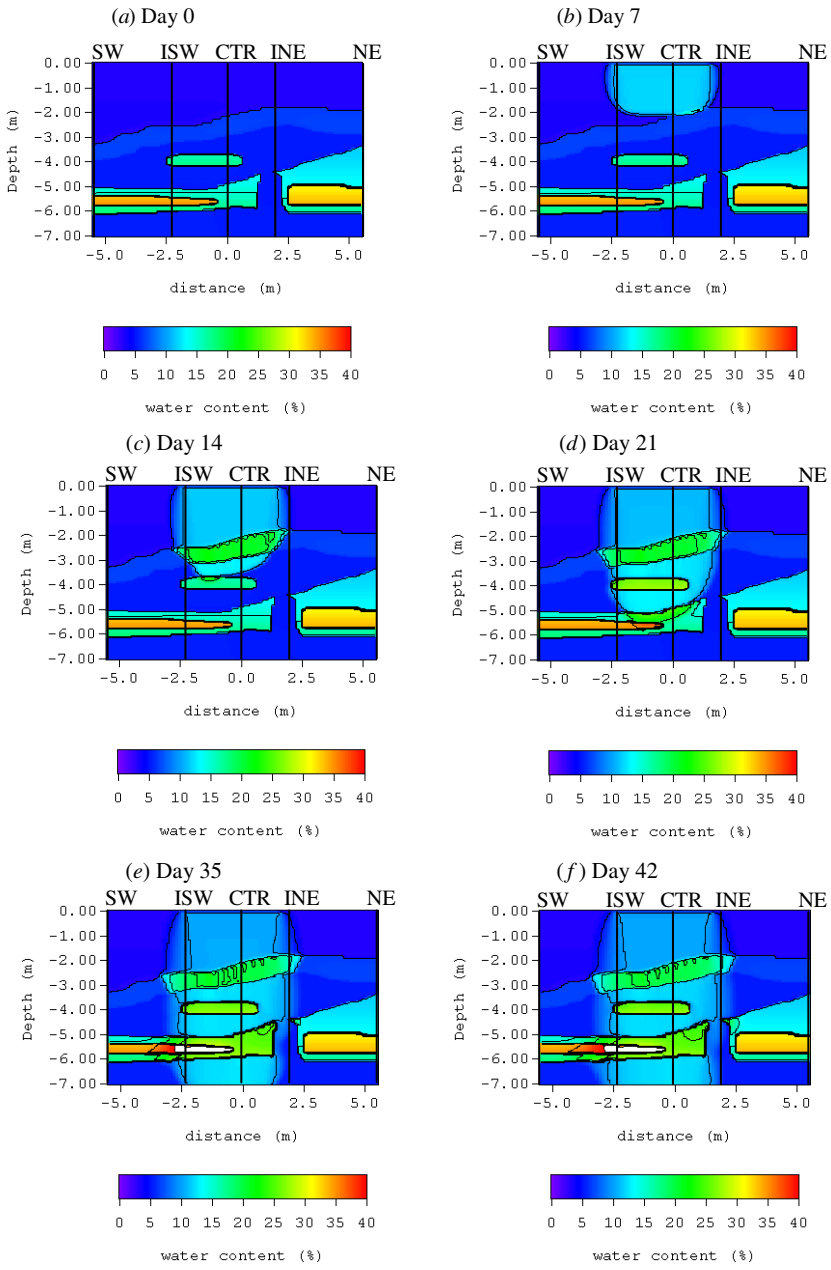

Figure 3. The modelled water content during the simulated water infiltration experiment provided by Hydrus-2D at (*a*) day 0, (*b*) day 7, (*c*) day 14, (*d*) day 21, (*e*) day 35, and (*f*) day 42. The solid lines indicate the locations of the boreholes used to simulate the XBGPR survey.

3. EM forward modelling

To simulate the EM wave-propagation phenomenon, we employed a staggered-grid FDTD solution to Maxwell's equations, developed by Holliger and Bergmann (2002). Holliger and Bergmann (2002) used the solution, which solves Maxwell's equations in a 2D cylindrical coordinate system, to analyse the response of XBGPR by assuming rotational symmetry with respect to the z-axis. To simulate radar-wave propagation using the FDTD approach, researchers must define the dielectric constant and electrical conductivity everywhere in space on a Cartesian grid (e.g. Lambot *et al* 2006, Kowalsky *et al* 2005). We defined these properties with a petrophysical model that determines soil electrical properties from the modelled water content. Various petrophysical models including lab-measured relationships and theoretical models have been proposed in the previous research works (e.g. reviews and examples have been given by Lesmes and Friedman (2005), Kowalsky *et al* (2005), and Lambot *et al* (2006)). Since most of the petrophysical models are site-specific and sensitive to soil properties, we use results from the lab and field measurements at the STVZ site in our research.

Owing to the presence of iron oxide minerals at the STVZ site, Alumbaugh *et al* (2002) suggested an empirical equation

$$\theta = 0.0136k_a - 0.033 \qquad (1)$$

for the relationship between the water content and the TDR-measured dielectric constant at the STVZ site. The dielectric constant, k_a, was estimated through an application of

equation (1) to the volumetric water content, θ, that had resulted from unsaturated-flow modelling. The electrical conductivity was estimated by applying a power-law function that is similar to Archie's empirical equation (Archie 1942) which describes the relationship between the bulk soil conductivity, σ, and the pore water conductivity, σ_w, for saturated soils. In unsaturated soils, Archie's law is written as

$$\sigma = aS^n\phi^m\sigma_w, \tag{2}$$

where ϕ is the porosity, S is the saturation, and a, n, m are the constants for a particular soil type (Telford *et al* 1991). Archie's equation assumes that the bulk conductivity is affected by the fluid conductivity, the porosity and the saturation. LaBrecque *et al* (2002) found that rather than using Archie's law directly, it was better to employ a simpler exponential relationship where the main parameter is the residual moisture content, which is in turn dependent on the grain-size distribution. In this study, we adopted a single power-law function similar to that of LaBrecque *et al* (2002). The relationship between bulk conductivity and water content can then be described as

$$\sigma = a \cdot \theta^b, \tag{3}$$

where σ is the bulk conductivity, θ is the volumetric water content, and a and b are the empirical constants that were determined through a comparison of measured conductivity to neutron-derived water content. Although the parameters a and b may vary spatially and are inconsistent between the pre-water-infiltration experiment and the post-water-infiltration experiment (LaBrecque *et al* 2002), we used the same values here in order to keep a simple, consistent physical relationship between water content and attenuation throughout the infiltration simulation. Here, we determined $a = 0.11$ and $b = 0.81$ from the neutron-estimated water content and from the induction logs taken before initiation of the infiltration (Brainard *et al* 2004).

We simulated XBGPR surveys by using a multi-offset gather configuration with a data-acquisition spacing of 0.25 m and a 100 MHz signal source. Because the majority of the observable changes in the flow modelling occurred only within the inner two well pairs, we saved computation time by simulating only the radar responses in the two centre borehole pairs, ISW–CTR and CTR–INE. The angles of the transmitting antenna to the receiving antenna were limited to 35° as in the field-data processing procedures. These angles were limited due to two major problems that are encountered when attempting to take advantage of the wide angular coverage in most field XBGPR practices (Irving *et al* 2007). First, the arrival times of high transmitter–receiver angles greater than 35–50° are often very difficult to pick because of low signal-to-noise ratios (e.g. Peterson 2001, Holliger and Bergmann 2002). Second, the borehole high-angle data may have faster travel paths through the air–soil interface along the borehole and are often incompatible with the lower-angle data available, causing significant numerical artefacts in the resulting tomograms (Peterson 2001, Alumbaugh *et al* 2002, Irving and Knight 2005). Although Irving *et al* (2007) propose a modified strategy to improve the high-angle data for inversion, as yet the strategy has limited improvement compared to the common exclusion approach. As a result, we excluded high-angle travel-time data from cross-hole GPR inversions as those in most field practices (e.g. Alumbaugh *et al* 2002, Linde *et al* 2006). However, one should bear in mind that such an approach comes at the cost of reduced resolution, especially for regions near boreholes, in the horizontal direction if two boreholes are far apart.

From the field XBGPR measurements, we found a minimum wavelength of 0.89 m when we assumed a frequency of 100 MHz. Therefore, to stabilize FDTD modelling results, we chose a grid spacing of 0.0625 m × 0.0625 m as suggested in Holliger and Bergmann (2002) for forward modelling. We transformed the unsaturated-flow model into the EM grid system by averaging the parameters of adjacent vertical cells while dividing horizontal cells in half. This discretization resulted in 56 833 cells in a model, and each simulation required approximately 1.5 h to be completed using a Pentium III-850 PC on a Windows NT 4.0 platform.

4. Inversion of the synthetic XBGPR data

4.1. Inversion methodology

The first-arrival time (travel time) and amplitude of the received EM signals are used as data to invert for velocity and attenuation. For this experiment, the inversion domain consists of a discrete 2D grid of cells that are 0.25 m on both sides. The travel time and attenuation for each GPR 'time-series' first arrival can be represented as (Sharma 1997, Jackson and Tweeton 1996)

$$t_i(\text{or } \alpha_i) = \sum_{j=1}^{M} p_j d_{ij}, \tag{4}$$

where t_i (α_i) represents the total travel time or attenuation for the ith ray path, p_j is the average slowness or attenuation of the jth cell, d_{ij} is the distance of the ith ray path within the jth cell, and M represents the number of cells passed through by the ith ray path. The attenuation of each ray path can be calculated as

$$\alpha_i = -\ln \frac{A_i}{A_0}, \tag{5}$$

where A_0 is the amplitude of the transmitted waveform, and A_i is the received amplitude.

Factors other than intrinsic attenuation, including geometrical spreading and the radiation pattern of the transmitter and receiver, also affect the amplitude measured by the GPR system (Peterson 2001). The transmitting antenna can be thought of as a dipole that radiates EM waves in a spherical geometry. Thus the measured amplitude in a homogeneous medium can be represented as

$$A_m = A_i(\cos\theta/R), \tag{6}$$

where A_i is the amplitude that only depends on the intrinsic attenuation for the ith ray path, θ is the angle measured from the horizontal to the ray path, and R is the distance between the transmitter and receiver antennas.

The commercial inversion code GeotomCG^{TM} (GeoTom 1998), which is widely used in cross-hole radar tomography

(e.g. Fullagar *et al* 2000, Tronicke *et al* 2001, Becht *et al* 2004), was used to produce images of velocity and attenuation from travel time and normalized amplitude measurements. GeotomCG^{TM} employs a simultaneous iterative reconstruction technique (Jackson and Tweeton 1996) and implements ray bending methods to generate tomographic images. One can select straight-ray (SR) or curved-ray algorithms for the inversion in the GeotomCG^{TM} software. The ray bending algorithm adopted by GeotomCG^{TM} improves the original algorithm proposed by Um and Thurber (1987) for imaging sharp contrasts of the velocity field (Becht *et al* 2004). For velocity inversions, we did not perform additional regularization and terminated the iteration process when the difference of the RMS residuals was under 0.1 ns. For the attenuation inversion, the inversion iterations were terminated when the difference of the RMS residuals was less than 0.01 Np.

4.2. The inverted images

We examined three cases to analyse the resolution of XBGPR tomograms. Initially for the EM FDTD forward modelling and inversion, we used the pre-infiltration steady-state model from the unsaturated-flow modelling. This allowed us to investigate the method's resolution of water content and attenuation under the field condition. In the second case, we used the results of the transient unsaturated-flow modelling to analyse the resolution of time-varying changes in attenuation and in water content during water infiltration. In the third case, we synthesized an early-time and a late-time model to examine the resolution of XBGPR for imaging saltwater infiltration under the flow steady-state conditions in the vadose zone.

Case 1: pre-infiltration (steady-state) XBGPR imaging. In case 1, we used the results of the unsaturated-flow modelling at day 0 as the input model for the FDTD forward modelling. We transformed water contents into dielectric constants and conductivities by using equations (1) and (3), respectively, for the FDTD EM forward modelling. The synthetic data from the FDTD modelling were then inverted with the GeotomCG^{TM} inversion code. Dielectric constants were computed from the inverted velocities, and then converted back into water contents on the basis of equation (1). The root-mean square (RMS) residual errors of velocity tomograms are 0.76 and 0.67 ns for SR and curved-ray inversions, respectively. The RMS errors of attenuation tomograms for SR and curved-ray inversions are 0.22 and 0.26 Np, respectively.

Figure 4 shows both the water contents and the attenuation-input model derived from unsaturated-flow modelling (figures 4(*a*) and (*d*)) along with tomograms resulting from SR and curved-ray inversions on the FDTD-synthesized data (figures 4(*b*), (*c*), (*e*) and (*f*)). A comparison between figures 4(*b*) and (*c*) indicates that the clay layers with higher water content can be resolved through the use of SR and curved-ray inversions. The water content was overestimated for about 3–6% in the sand layers and underestimated for about 2–3% in the clay layers for the SR inversion. For the curved-ray inversion, the water content was overestimated for about 3–6% in the sand layers and underestimated for about 1–2% in the clay layers. Moreover, both the SR and curved-ray inversion methods do not resolve the 1 m wide discontinuity of clay at a depth of 5 to 6 m between the CTR borehole and the INE borehole in the input model. This finding suggests that the antenna configurations and the data processing strategies, such as limited angles, employed here are insensitive to horizontal variations in water content and that they are, therefore, unable to resolve the 1 m discontinuous gap within the clay layer.

Figure 4(*d*) shows the input attenuation model for FDTD modelling, and figures 4(*e*) and (*f*) are the inverted attenuation images of SR and curved-ray inversions, respectively. Compared to the water-content image, the inverted attenuation image provides poorer continuity of the fine-grained layer between a depth of 5 and 6 m. Figures 4(*e*) and (*f*) also indicate that the high attenuation region at a depth of 4 m, which corresponds to a thin clay layer in the input model, is truncated in the centre of the imaging region, resulting in two isolated anomalies near the CTR borehole and the ISW borehole. A comparison between figures 4(*e*) and (*f*) and the input model reveals that the attenuation within the lower layer is overestimated near the boreholes but underestimated between them.

In addition, the curved-ray inversion seems to produce worse estimation than the SR inversion in this case. Theoretically, the first-arriving EM wave-fronts tend to travel through high-velocity regions rather than low-velocity regions. This makes the ray paths in an inhomogeneous medium tend to curve around the low-velocity regions, and thus they are no longer straight lines. Attenuation inversion is conducted with the ray paths constructed with the ray bending algorithm in the velocity inversion. It should be more realistic and accurate to use the curved-ray inversion (Alumbaugh *et al* 2002). Jackson and Tweeton (1996) pointed out that the ray-based algorithm may fail for the attenuation inversion in media with strong heterogeneities. We will discuss the reasons that may cause the worse estimations of curved-ray inversion later in section 5.

Case 2: the water-infiltration (transient-state) experiment. In the transient-state cases, the ray paths of EM waves may vary in different infiltration stages and it is difficult to correctly apply the corrections that account for the geometric spreading and the antenna radiation effects through a curved path. In addition, we found that the attenuation curved-ray inversion produced worse results than the SR inversion. As a result, we used only the SR method for the inversion of time-lapse images during water infiltration. The RMS residual errors of the inversion results at different stages are shown in table 2.

We next analysed the resolution and the accuracy of the time-lapse imaging process by inverting the FDTD synthetic data, and differencing the results against the day 0 images given in figures 4(*c*) and (*d*). Figures 5(*a*) to (*e*) show the time-lapse difference images for the model and the inverted FDTD results at days 7, 14, 21, 35, and 42, respectively. Images between 1 and 7 m depth are shown because radar signal data near

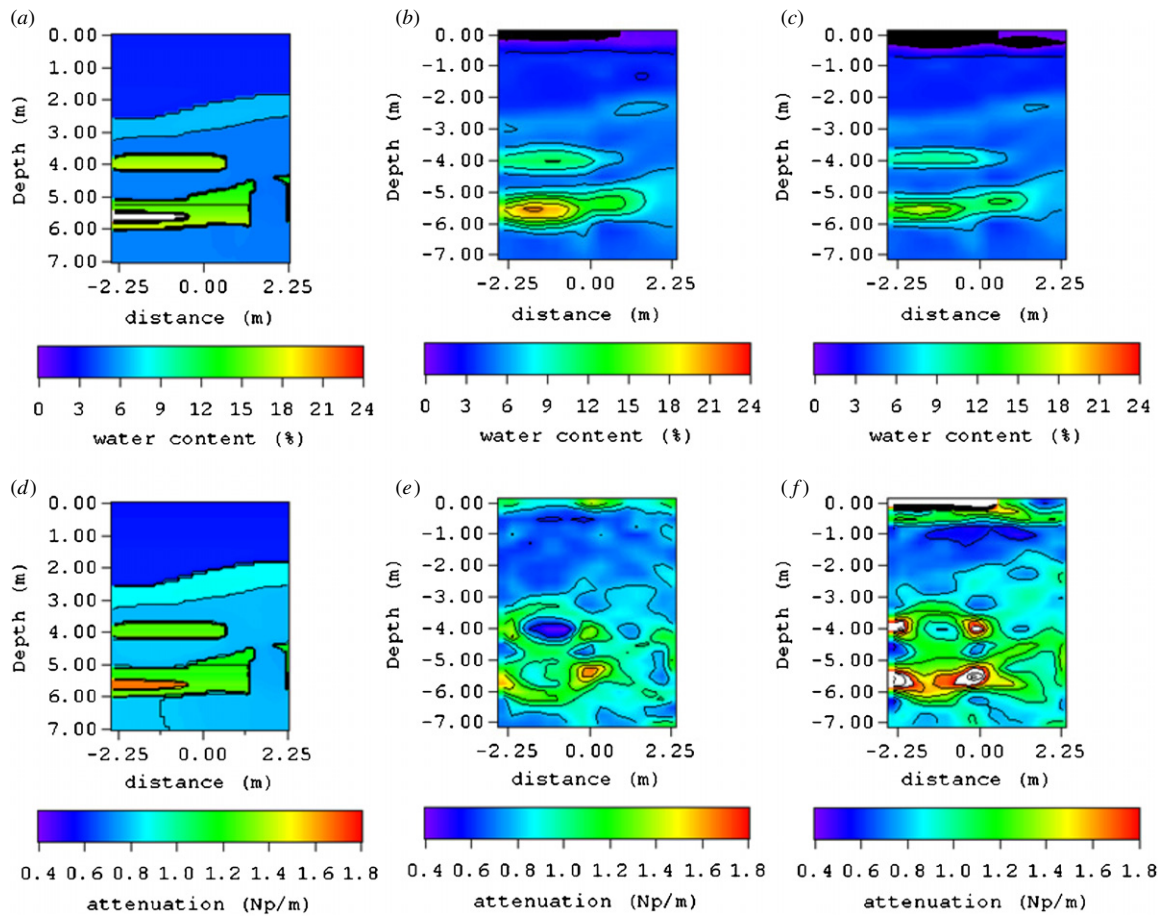

Figure 4. (*a*) The water content model before water infiltration is initiated, (*b*) the inverted water content image using curved-ray inversion of the FDTD results, and (*c*) the inverted water content image using SR inversion of the FDTD results. (*d*) The attenuation input model for FDTD modelling before water infiltration is initiated, (*e*) the inverted attenuation image using curved-ray inversion, and (*f*) the inverted attenuation image using SR inversion.

Table 2. The inversion residual error in different modelling stages.

	RMS residual error	
Infiltration stage	Velocity inversion (ns)	Attenuation inversion (Np)
Pre-infiltration	0.76	0.22
Water infiltration: day 7	0.77	0.35
Water infiltration: day 14	0.82	0.36
Water infiltration: day 21	0.64	0.33
Water infiltration: day 35	0.68	0.33
Water infiltration: day 42	0.67	0.33
Salt infiltration: early time	0.3	0.39
Salt infiltration: late time	0.28	0.38

the earth surface were saturated with reflected and air-wave noise.

In figure 5(*a*), the water-content difference image resulting from inversion of the FDTD modelling shows that the water plume is, in general, recovered after day 7. On the other hand, the inverted attenuation image shows that an isolated region of increased attenuation appeared at 2 m depth near the front of the water plume at day 7. This 'bull's eye'-like structure appears to be an artefact, and similar to the 'snow-plow' structure (Chang *et al* 2004) observed in the imaging of the field data during the water-infiltration stage, indicates that the structure observed is an artefact resulting from attenuation inversion.

Figure 5(*b*) shows that the differences in water content and attenuation continued to increase 14 days after infiltration had begun. The volumetric water content increased to about 12% in a concentrated zone between 2 and 3 m depth. In comparison with the input model, it appears that the region of increased water content could be resolved, although the peak volumetric water-content increase was about 4% less than the true value. However, the attenuation difference image that resulted from inversion of the FDTD-produced synthetic data does not provide as clear a picture of the infiltration process as the water content image at day 14. The attenuation difference image shows that local maximum and minimum zoning of attenuation existed at between 1 and 4 m depth.

Inverted water-content and attenuation difference images at days 21, 35 and 42 (figures 5(*c*)–(*e*)) verify the earlier results that increases in water content can be better resolved than the attenuation images. Compared with the input model, the inverted water-content differences were about 2% to 4% less than those in the input model, and water-content increases in the 4 m deep clay layer barely appeared in the inverted FDTD images at days 35 and 42. The inverted water difference image

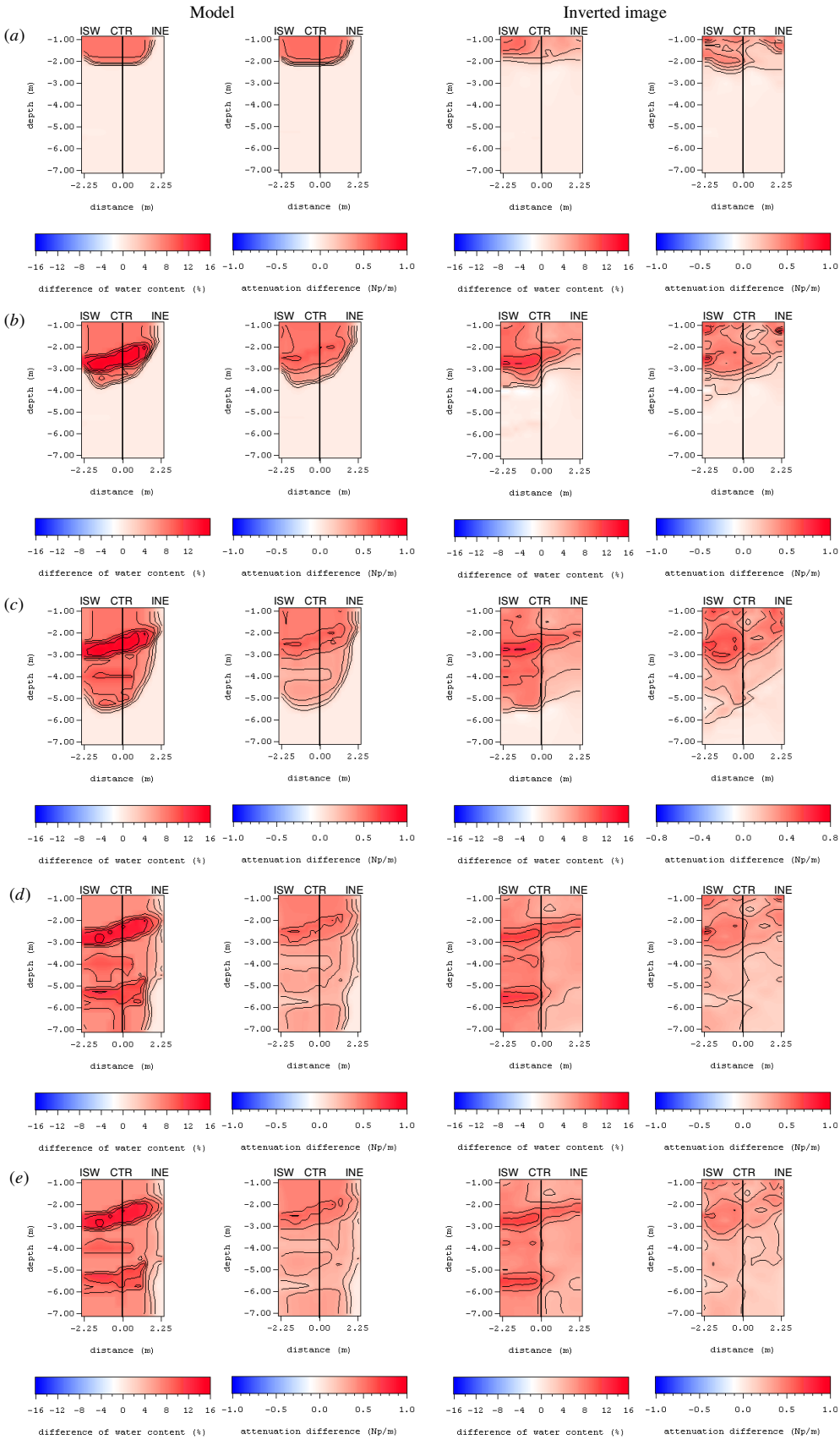

Figure 5. Water content and attenuation of the input model (left) and inverted FDTD images (right): (*a*) 7 days after the infiltration was initiated, (*b*) 14 days after the infiltration was initiated and (*c*) 21 days after the infiltration was initiated. The water content and attenuation of the input model (left) and the inverted FDTD images (right): (*d*) 35 days after the infiltration was initiated and (*e*) 42 days after the infiltration was initiated.

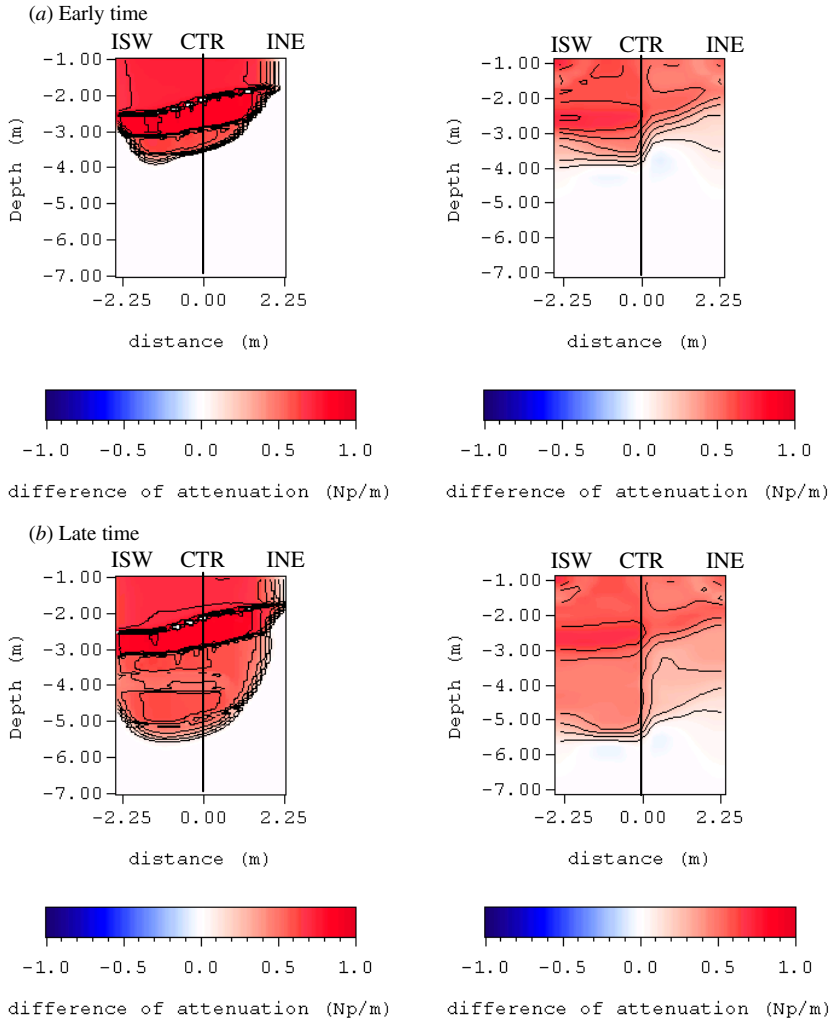

Figure 6. (*a*) Left: the attenuation difference of the model simulating 'early-time' salt infiltration, right: the difference image of attenuation inverted from the FDTD result of the early-time model of salt infiltration. (*b*) Left: the attenuation difference of the model simulating 'late-time' salt infiltration, right: the difference image of attenuation inverted from the FDTD result of the late-time model of salt infiltration.

also showed that the right part of the water plume between the CTR borehole and the INE borehole was underestimated in relation to its left part between the CTR borehole and the ISW borehole, so that the shape of the inverted water plume seems to be truncated in the CTR borehole.

In figures 5(*c*) to (*e*), the development of the higher attenuation region can be correlated to the progress of the water plume in the input model. Although the attenuation difference images in figures 5(*c*) to (*e*) illustrate the location of the high attenuation zone, the bull's-eye artefact also appears between 2 and 3 m depth, as in the 7 day and 14 day images. Compared with the input model, the attenuation increase in the centre of the bull's-eye structure is underestimated for about 0.1 Np m^{-1}. However, the same artefact does not appear in the water-content image as in the attenuation image. Because FDTD modelling represents the 'true-physics' conditions, it appears that the velocity imaging using straight rays tends to slightly overestimate the velocity in slower regions, thus underestimating the moisture content, while the attenuation SR imaging results in artefacts owing to incorrect physical assumptions.

Case 3: the saltwater-infiltration experiment. Unfortunately, there were no measurements made on the core samples collected during drilling to define the soil parameters required for transport modelling, and thus the salt infiltration was not simulated explicitly. In order to analyse the resolution of time-lapse attenuation imaging for solute monitoring, EM models crudely simulating the conditions observed during the salt pulse were synthesized by combining the input models employed in case 2. The EM cross-section resulting from applying the petrophysical conversions to the day 42 flow model results shown in figure 3(*f*) was employed as the background to represent steady-state flow conditions. Conductivity perturbations associated with days 14 (figure 3(*c*)) and 21 (figure 3(*d*)) were then added to the background while leaving the dielectric constant unchanged. That is, the conductivity perturbations corresponding to the attenuation increases shown in figures 3(*c*) and (*d*) were added onto the conductivity model for day 42. By increasing conductivity while leaving the dielectric constant alone, we would be able to increase attenuation significantly but not affect the velocity. Although the dispersion of the salt

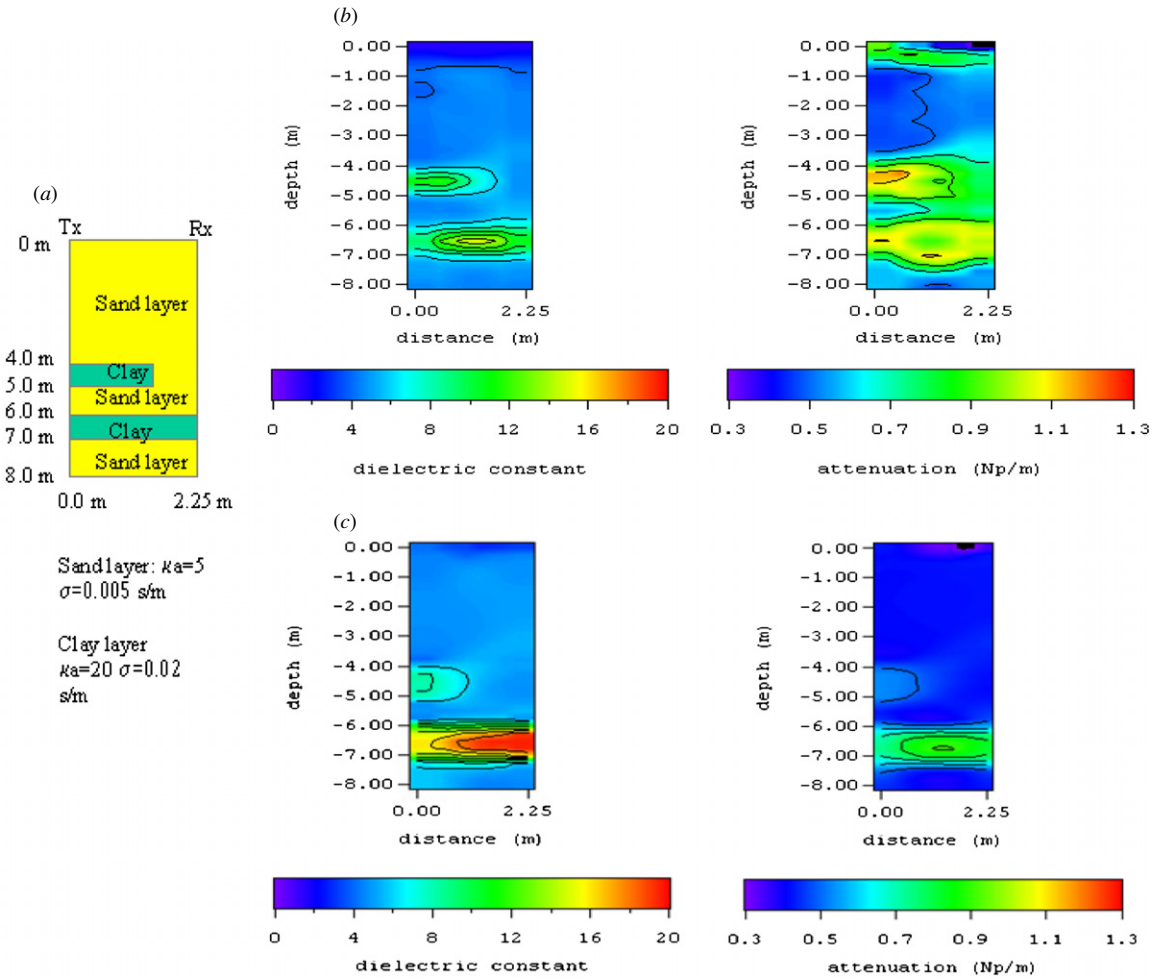

Figure 7. (*a*) The input model with two 1 m thick clays in an 8 m thick sand layer. (*b*) The inverted dielectric constant and attenuation images for the synthesized data of FDTD modelling. (*c*) The inverted dielectric constant and attenuation for the data synthesized with SR modelling.

plume is not accounted for, this approach produces models which crudely imitate the transient saltwater plume at two different times during the salt infiltration without performing contaminant transport modelling.

A comparison of the inverted FDTD modelling results with the input model (figure 6) shows that the images indicate a region of increased attenuation at a depth of 2–3 m corresponding to the location of the saltwater. The attenuation differences inverted from FDTD modelling are about 0.2–0.3 Np m^{-1} less than those of the input model. In addition, note that the bull's-eye artefacts that were seen in the attenuation images in figure 5 are not generated here. The likely reason why the attenuation images of the FDTD results appear free from artefacts in this case is that the water content, and thus the dielectric constant and velocity, is kept constant for both the pre- and post-saltwater infiltration cases. Therefore the ray paths are the same for the two sets of images used to produce the time-lapse difference. This suggests that the SR attenuation inversion is able to recover the salt plume through the attenuation difference images if the system is at the steady-state flow conditions, and the only difference is the introduction of a conductive tracer.

5. Discussion

To further investigate the reason for the bull's-eye artefact in the attenuation images in cases 1 and 2, we produced another synthetic radar data set by using a simple model with two 1 m thick clays in an 8 m thick sand layer (figure 7(*a*)). Based on the SR assumption, the SR forward modelling calculated the travel time and attenuation for each transmitter and receiver pair by adding up the slowness (time needed for an EM pulse to pass through a cell) and attenuation along each ray path (equation (4)) within the same 2D discrete model as in the FDTD simulation. The synthetic data from the FDTD and SR forward modelling were inverted with the same inversion code, GeotomCG^{TM}. Figures 7(*b*) and (*c*) show the inverted images of the FDTD modelling and SR modelling, respectively. Compared with the input model in figure 7(*a*), the attenuation image in figure 7(*b*) indicates that the bull's eye artefact appears in the lower clay layer. On the other hand, figure 7(*c*) shows that the inversion can correctly resolve the lower clay layer at 6 to 7 m depth if EM waves propagate through the SR paths. Figure 7(*c*) also shows that the inversion tends to underestimate both the dielectric

constant, or the calculated water content, and attenuation near the boreholes.

Compared with the images in figure 7(*b*), no artefacts appear in either the dielectric constant or the attenuation images in figure 7(*c*). Therefore, it is likely that the bull's-eye artefact resulted from the application of SR assumptions to the true physics.

Figure 8(*a*) is the FDTD-modelled ray traces at different receiver positions in time domain when the transmitter position was at 6.5 m depth. Figure 8(*b*) illustrates the calculated travel time of the XBGPR signal for the FDTD modelling (after correction for geometrical factors) and the SR modelling. In figure 8(*b*), the travel-time data of FDTD modelling show a similar trend to the SR modelling data. Both the FDTD results and the SR results show that the data with receiver positions in the clay layer have a longer travel time than those with receiver positions in the sand layer. The maximum difference between the FDTD-estimated travel time and the SR travel time occurs when the receiver position is at the clay–sand boundary.

Figure 8(*c*) shows the attenuation for the FDTD modelling (after correction for geometrical factors) and the SR modelling when the transmitter was at 6.5 m depth. The calculated attenuation of FDTD modelling exhibits a trend that differs from that of the attenuation estimated with SR assumptions. Unlike predictions derived from the SR modelling, the FDTD-estimated attenuation for receiver positions located in the clay layer is less than those data with receiver positions in the sand layer. Also the FDTD synthetic signals for the receivers located in the clay layer exhibited a less attenuated waveform than the others in figure 8(*a*). In figure 9(*a*), we plotted the first-arrival time of the GPR pulse in the profile. Two faster curved-ray paths passing around the clay layer can be identified in figure 9(*a*). On the other hand, the FDTD-simulated results show a three-lobe pattern of low attenuation zones in figure 9(*b*). Besides the two lobes associated with the aforementioned curved-ray paths, the GPR EM pulse waves are travelling through the clay layer and arriving at the receivers in the clay layer later with less attenuated amplitudes.

The distribution of FDTD-estimated attenuation in figure 9(*b*) suggests that the clay layer, in fact, served as a dielectric waveguide when the transmitter antenna was placed in the clay layer. The received EM-wave signals for the receivers at the sand–clay boundary have higher attenuation, yet the received EM-wave signals inside the clay layer are less attenuated. Thus, if the SR assumption is used directly for inversion of the FDTD synthetic or the true field data, a bull's-eye artefact, such as those shown in the attenuation images in figure 4, will result in a low attenuation region surrounded by an overestimated high attenuation region at the location of the clay layer.

In comparison with figure 9(*b*), figure 9(*a*) shows that the EM wave-front had a longer travel time and lower attenuation at a depth of 6.5 m in the receiver borehole than the adjacent receiver positions at 6.25 and 6.75 m. The pattern of travel time and of attenuation indicates that an extra energy loss existed when the EM wave crossed the sand–clay boundary. Fresnel's equations describe the change of the reflected and

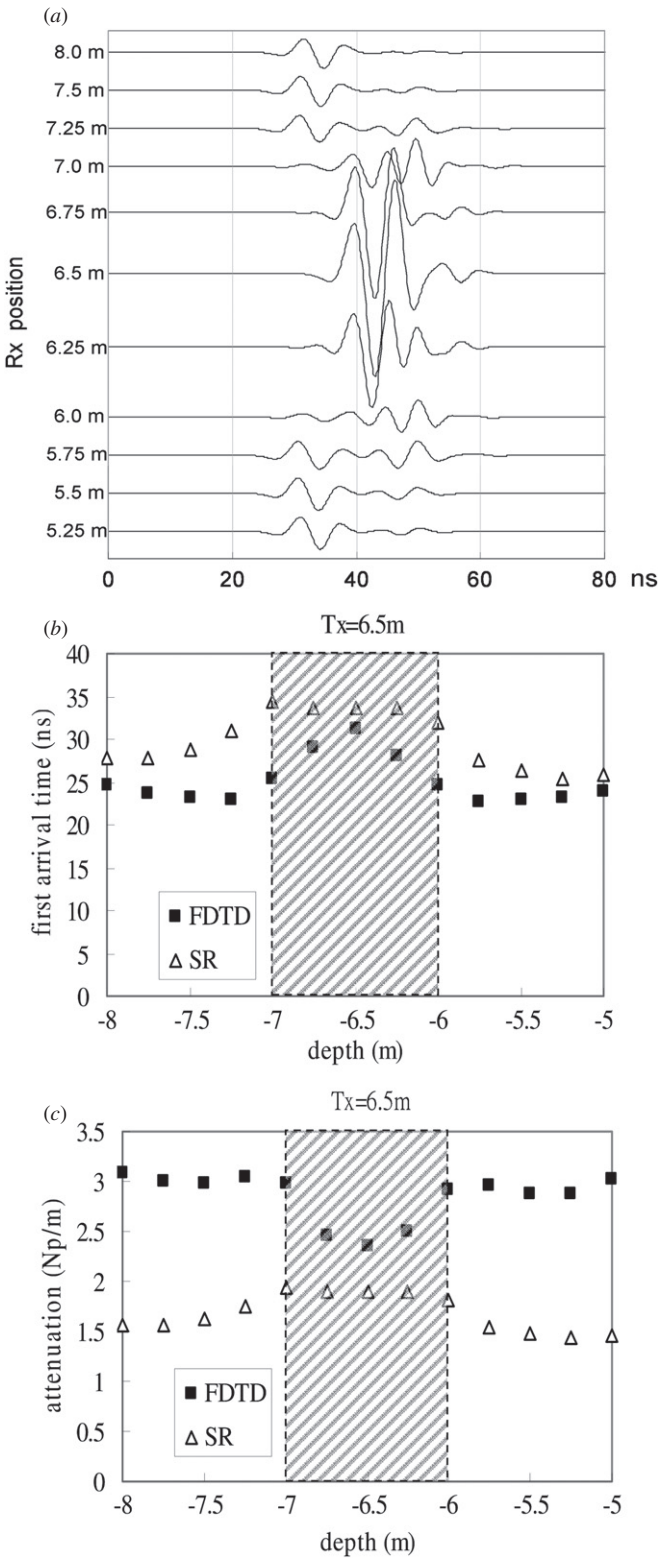

Figure 8. (*a*) The FDTD simulated ray traces received at different receiver positions with transmitter position fixed at 6.5 m. (*b*) Calculated first-arrival time from the FDTD and the SR forward modelling with transmitter position at 6.5 m for the input model in figure 4(*a*). (*c*) Calculated total attenuation of the FDTD results (after correction for geometrical factors) and estimated total attenuation of the SR forward modelling with transmitter position at 6.5 m. The shaded area represents the location of the clay layer in the input model.

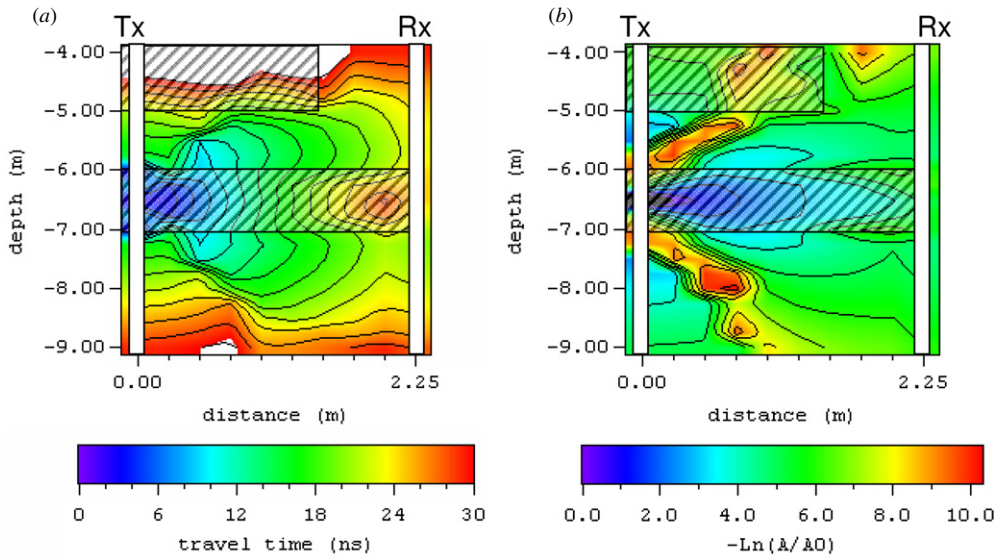

Figure 9. (*a*) FDTD-calculated travel time of the GPR EM pulse wave for transmitter position at 6.5 m. (*b*) FDTD-calculated attenuation of the GPR EM pulse wave for transmitter position at 6.5 m. (The shaded area represents the locations of clay layers in the input model. Tx and Rx mark the locations of the transmitter borehole and the receiver borehole, respectively.)

the transmitted amplitudes for perpendicularly polarized EM waves,

$$r = \frac{E_{0r}}{E_{0i}} = \frac{[v_t \cos\theta_i - v_i \cos\theta_t]}{[v_t \cos\theta_i + v_i \cos\theta_t]} \tag{7}$$

and

$$t = \frac{E_{0t}}{E_{0i}} = \frac{2v_t \cos\theta_i}{[v_t \cos\theta_i + v_i \cos\theta_t]}, \tag{8}$$

where r is the reflection coefficient, t the transmission coefficient, E_{0i} the incident electric field, E_{0r} the reflected electric field, E_{0t} the transmitted (refracted) electric field, v_i the incident velocity, v_t the transmitted velocity, θ_i the angle of incidence and θ_t the angle of refraction.

Equations (7) and (8) illustrate that the EM waves crossing a sharp velocity boundary will give rise to an amplitude change of waveforms. Therefore, the reflection coefficients and the transmission coefficients should be taken into account in the ray-based attenuation inversion processes so that the inversion of intrinsic attenuation is correct.

In addition, the symmetrical-travel-time pattern in figure 9(*a*) suggests that the receiver located in the centre of the clay layer would have multiple ray paths. The integration of wave-fronts arriving at the same time through different ray paths results in a less attenuated EM waveform received in the centre of the clay layer. The findings proved that the velocity structures can be well restored with the curved ray inversion methods; however, the attenuation structure can be correctly resolved only if multiple ray paths are considered in the same curved-ray-inversion algorithm. Therefore, one should be careful in using the XBGPR attenuation images for water infiltration monitoring if guided wave phenomenon in the horizontal clayey layer is expected.

On the other hand, in case 3 we had increased conductivity and left the dielectric constant in order to increase attenuation significantly but not affect the velocity field. We found no 'bull's eye' structures in either the early-time or late-time attenuation difference images. The findings were similar to our previous observations of the salt fluid infiltration experiments at the STVZ site (Chang *et al* 2006). Since the velocity field remains unchanged, the perturbation of the conductivity and subsequent intrinsic attenuation can be inverted correctly with the inversion based on the ray theory. Therefore, the XBGPR attenuation difference images can still provide correct information for the distribution of the salt plume in the salt infiltration experiment under a steady state flow.

In this study we examined the curved-ray and straight inversion for GPR XB tomography, and concluded that further correction for the scattering effect and multiple ray paths should be taken into account in order to invert attenuation accurately. One other possible solution to account for the problem from the ray-based inversion is the full waveform inversion with FDTD forward modelling (e.g. Ernst *et al* 2007). However, the full waveform inversion comes at a cost of huge computing time and the computer resolving power needed. For instance, the ray-based inversions required only about 30 min on a single computer with a 32-bit Intel Xeon 2.4 GHz processor. The full-waveform inversions required more than 12 h on a workstation with *N*+1 64-bit AMD 244 1.8 GHz processors (where *N* is the number of transmitters) (Ernst *et al* 2007). In addition, the real field data may also carry a lot of near surface noise and would not be able to be filtered out. These hamper the application of full waveform inversion in the field practices, especially in the time-lapse monitoring experiments such as the one at the STVZ site.

6. Conclusion

In this study, we conducted a test incorporating unsaturated-flow modelling, EM forward modelling and data inversion to analyse XBGPR resolution and accuracy in the analysis of the field data collected at the STVZ site. Three different cases

were examined in the test. In case 1, we coupled a steady-state unsaturated-flow model with EM forward modelling to analyse the resolution of XBGPR for field data that have irregular geometries. Water contents were transformed into dielectric constant and conductivity to be used in the FDTD EM forward modelling. The FDTD synthetic data were inverted with the damped least-squares method. In comparison with the input model, the inverted water content was overestimated by about 3–6% in the sand layers and underestimated by about 1–2% in the clay layers. Moreover, the water-content tomogram does not resolve the 1 m wide discontinuity at a depth of 5 to 6 m between the CTR borehole and the INE borehole. The inverted attenuation image provides poorer resolution than the water-content image for both the fine-grained layer at 4 m and the fine-grained layer between a depth of 5 and 6 m. In addition, an artefact like the 'bull's eye' structure appears at the location of the lower clay layer in the attenuation tomograms when the SR assumption is applied in the attenuation inversion. Compared to the input model, the attenuation tomogram reveals that the attenuation within the lower layer is overestimated near the boreholes but slightly underestimated between the boreholes.

In case 2, time-lapse EM models were created from the results of the unsaturated-flow modelling, and the SR damped least-squares inversion method was employed for both water content and attenuation estimation. Comparing the water-content difference images generated from the FDTD results with the input model shows that the SR inversion can resolve the developing water plume in a time-lapse sense, although the radar wave may actually travel along a curved path. On the other hand, the inverted attenuation image shows that an isolated region of increased attenuation appeared at 2 m depth near the front of the water plume at day 7. This structure appears to be a truncated 'bull's eye' artefact that was found only in the attenuation images in both case 1 and case 2. The artefact is similar to the 'snow-plow' structure (Chang *et al* 2002) observed in the imaging of the field data during the water-infiltration stage, and indicates that the structure observed is an artefact by attenuation inversion.

Although no measurements required for transport modelling were made on the STVZ core samples, we built a synthetic early-time model and a late-time model to analyse the accuracy and resolution of XBGPR attenuation imaging for the solute infiltration under a flow steady state in case 3. The results show that the attenuation anomaly images indicate a region of increased attenuation at a depth of 2–3 m corresponding to the location of the saltwater. In addition, the bull's-eye artefacts that were seen in case 2 are not generated here. The likely reason is that the system is in a flow steady state and therefore the ray paths are kept the same during the salt infiltration period. This suggests that the SR inversion is able to resolve the salt plume through the attenuation anomaly images if the system is in the steady-state flow condition, and the only difference is the introduction of a conductive tracer.

A further investigation of the bull's-eye artefact in the attenuation images shows that the clay layer, in fact, serves as a dielectric waveguide when the transmitter is located in the clay layer. The received EM-wave signals for the receivers at the sand–clay boundary have higher attenuation, yet the received EM-wave signals inside the clay layer are less attenuated. Thus if the SR assumption is used directly for the inversion of the FDTD synthetic or the true field data, it will result in a bull's-eye artefact with a low attenuation region surrounded by an overestimated high attenuation region at the location of the clay layer. The reason for a less attenuated waveform in the centre of the clay concerns the multi-ray paths from the transmitter. The integration of wave-fronts arriving at the same time through different ray paths results in a less attenuated EM waveform received at the receiver in the centre of the clay. Our findings also proved that the curved ray may be better in describing the true ray paths. Thus, with the curved-ray inversion, one should be able to get more accurate inverted water content than with the SR inversion. In addition, because the reflection–refraction coefficient and the multi-ray paths affect the amplitudes of the received EM waveforms, attenuation can be resolved correctly only if the factors of the refraction–reflection coefficient and the multi paths are taken into account in the curved-ray-inversion algorithm.

Acknowledgments

We are grateful to National Science Council of Taiwan who funded this research through research grant under contract 94-2116-M-041-001. We also would like to thank Dr Klaus Holliger at the University of Lausanne for providing the EM forward modelling source code.

References

Alumbaugh D, Chang P Y, Paprocki L, Brainard J R, Glass R J and Rautman C A 2002 Estimating moisture contents using cross-borehole ground penetrating radar: a study of accuracy and repeatability in context of an infiltration experiment *Water Resour. Res.* **38** 1309

Alumbaugh D, Paprocki L, Brainard J, C A and Rautman 2000 Monitoring infiltration within the vadose zone using cross-borehole ground penetrating radar *Proc. Symp. on the Application of Geophysics to Engineering and Environmental Problems* (Wheat Ridge, CO: Environmental and Engineering Geophysical Society) pp 273–81

Archie G E 1942 Electrical resistivity log as an aid in determining some reservoir characteristics *Trans. Am. Inst. Min. Metall. Pet. Eng.* **146** 54–62

Baker K E 2002 Investigation of direct and indirect hydraulic property laboratory characterization methods for heterogeneous alluvial deposits: application to the Sandia-Tech vadose zone infiltration site *MS thesis* New Mexico Institute of Mining and Technology, Socorro, NM, USA, 137 pp

Becht A, Tronicke J, Appel E and Dietrich P 2004 Inversion strategy in crosshole radar tomography using information of data subsets *Geophysics* **69** 222–30

Binley A, Winship P, Middleton R, Pokar M and West J 2001 High-resolution characterization of vadose zone dynamics using cross-borehole radar *Water Resour. Res.* **37** 2639–52

Brainard J R, Glass R J, Alumbaugh D L, Paprocki L, LaBrecque D J, Yang X, Yeh T-C J, Baker K E and Rautman C A 2004 The Sandia-Tech vadose zone facility: experimental design and data report of a constant flux infiltration experiment *Report* Sandia National Laboratories, Albuquerque, NM, USA

Chang P Y, Alumbaugh D L, Brainard J R and Hall L 2004 The application of ground penetrating radar attenuation tomography in a vadose zone infiltration experiment *J. Contam. Hydrol.* **71** 67–87

Chang P Y, Alumbaugh D L, Brainard J R and Hall L 2006 Cross borehole ground penetrating radar for monitoring and imaging solute transport within the vadose zone *Water Resour. Res.* **42** W10413

Day-Lewis F D, Harris J M and Gorelick S M 2002 Time-lapse inversion of crosswell radar data *Geophysics* **67** 1740–52

Ernst J R, Green A G, Maurer H and Hollige K 2007 Application of a new 2D time-domain full-waveform inversion scheme to crosshole radar data *Geophysics* **72** J53–64

Fullagar P K, Livelybrooks D W, Zhang P, Calvert A J and Wu Y 2000 Radio tomography and borehole radar delineation of the McConnell nickel sulfide deposit, Sudbury, Ontario, Canada *Geophysics* **65** 1920–30

Geotom 1998 *User Manual for GeotomCG and GeoTom3D* (Apple Valley, MN: GeoTom, LLC.,)

Holliger K and Bergmann T 2002 Numerical modeling of borehole georadar data *Geophysics* **67** 1249–57

Hubbard S S, Rubin Y and Majer E 1997 Ground-penetrating-radar-assisted saturation and permeability estimation in bimodal systems *Water Resour. Res.* **33** 971–90

Irving J D and Knight R J 2005 Effect of antennas on velocity estimates obtained from crosshole GPR data *Geophysics* **70** K39–42

Irving J D, Knoll M D and Knight R J 2007 Improving crosshole radar velocity tomograms: a new approach to incorporating high-angle traveltime data *Geophysics* **72** J31–41

Jackson M J and Tweeton D R 1996 3DTOM: three-dimensional geophysical tomography *Report of Investigations 9617* United States Department of the Interior, Bureau of Mines 84 pp

Johnson T C, Ruth P S, Barrash W and Knoll M D 2007 A field comparison of Fresnel zone and ray-based GPR attenuation-difference tomography for time-lapse imaging of electrically anomalous tracer or contaminant plumes *Geophysics* **72** G21–9

Kowalsky M B, Finsterle S, Peterson J, Hubbard S, Rubin Y, Majer E, Ward A and Gee G 2005 Estimation of field-scale soil hydraulic and dielectric parameters through joint inversion of GPR and hydrological data *Water Resour. Res.* **41** W11425

LaBrecque D, Alumbaugh D L, Yang Y, Paprocki L and Brainard J 2002 Three-dimensional monitoring of vadose zone infiltration using electrical resistivity tomography and cross-borehole ground penetrating radar *Three-Dimensional Electromagnetics (Methods in Geochemistry and Geophysics Series 35)* ed M S Zhdanov and P E Wannamaker (New York: Elsevier) pp 260–72

Lambot S, Slob E C, Vanclooster M and Vereecken H 2006 Closed loop GPR data inversion for soil hydraulic and electric property determination *Geophys. Res. Lett.* **33** L21405

Lesmes D P and Friedman S P 2005 Relationships between the electrical and hydrogeological properties of rocks and soils *Hydrogeophysics* ed Y Rubin and S Hubbard (New York: Springer) 532 pp

Linde N, Binley A, Tryggvason A, Pedersen L B and Revil A 2006 Improved hydrogeophysical characterization using joint inversion of crosshole electrical resistance and ground penetrating radar traveltime data *Water Resources Res.* **42** W12404

Paprocki L 2000 Characterization of vadose zone *in-situ* moisture content and an advancing wetting front using cross-borehole ground penetrating radar *MS Thesis* New Mexico Institute of Mining and Technology, Socorro, NM, USA 120 pp

Peterson J E 2001 Pre-inversion correction and analysis of radar tomographic data *J. Environ. Eng. Geophys.* **6** 1–8

Sharma P V 1997 *Environmental and Engineering Geophysics* (New York: Cambridge University Press) 475 pp

Simunek J and van Genuchten M T 1999 The HYDRUS-2D software package for simulating the two-dimensional movement of water, heat, and multiple solutes in variably-saturated media, version 2.0 U.S. Salinity Laboratory, Riverside, CA, USA

Telford W M, Geldart L P, Sheriff R E and Keys D A 1991 *Applied Geophysics* (New York: Cambridge University Press) 770 pp

Tronicke J, Tweeton D R, Dietrich P and Appel E 2001 Improved crosshole radar tomography by using direct and reflected arrival times *J. Appl. Geophys.* **47** 97–105

Um J and Thurber C 1987 A fast algorithm for two-point seismic ray tracing *Bull. Seismol. Soc. Am.* **77** 972–86